Accelerating Sulfur Redox Kinetics by Electronic Modulation and Drifting Effects of Pre-lithiation Electrocatalysts

Haimei Wang, Hao Yuan, Wanwan Wang, Xingyang Wang, Jianguo Sun, Jing Yang, Ximeng Liu, Qi Zhao, Tuo Wang, Ning Wen, Yulin Gao, Kepeng Song*, Dairong Chen, Shijie Wang, Yong-Wei Zhang*, John Wang**

Dr. H. M. Wang, X. Y. Wang, Dr. J. G. Sun, Dr. X. M. Liu, Dr. Q. Zhao, T. Wang, Y. L. Gao, Prof. J. Wang
Department of Materials Science and Engineering, National University of Singapore, Singapore117574, Republic of Singapore.
Email: msewangj@nus.edu.sg (J. Wang), sjg07@nus.edu.sg (J. G. Sun)

Dr. H. Yuan, Dr. J. Yang, Prof. Y-W. Zhang
Institute of High Performance Computing (IHPC), Agency for Science, Technology and Research (A*STAR), 1 Fusionopolis Way, #16-16 Connexis, Singapore 138632, Republic of Singapore
Email: zhangyw@ihpc.a-star.edu.sg (Y-W. Zhang)

Dr. W. W. Wang, Prof. S. J. Wang
Institute of Materials Research and Engineering (IMRE), Agency for Science, Technology and Research (A*STAR), 2 Fusionopolis Way, Innovis #08-03 Singapore 138634, Republic of Singapore

Prof. K. P. Song
Electron Microscopy Center, Shandong University, Jinan, Shandong 250100 China.
E-mail: kpsong@sdu.edu.cn (K. P. Song)

N. Wen, Prof. D. R. Chen
School of Chemistry and Chemical Engineering, Shandong University Jinan, Shandong 250100 China.

Prof. J. Wang
National University of Singapore (Chongqing) Research Institute, Chongqing Liang Jiang New Area, Chongqing 401120, China.

Abstract:

Efficient catalyst design is crucial for addressing the sluggish multi-step sulfur redox reaction (SRR) in lithium-sulfur batteries (LiSBs), which are among the promising candidates for the next-generation high-energy-density storage systems. However, the limited understanding of the underlying catalytic kinetic mechanisms and

the lack of precise control over catalyst structures pose challenges in designing highly efficient catalysts, which hinder the LiSBs' practical application. Here, drawing inspiration from our theoretical calculations, we propose the concept of precisely controlled pre-lithiation SRR electrocatalysts. The dual roles of channel and surface lithium in pre-lithiated 1T'-MoS_2 are revealed, referred to as the "electronic modulation effect" and "drifting effect", respectively, both of which contribute to accelerating the SRR kinetics. As a result, the thus-designed 1T'-Li_xMoS_2/CS cathode obtained by epitaxial growth of pre-lithiated 1T'-MoS_2 on cubic Co_9S_8 exhibits impressive performance with a high initial specific capacity of 1049.8 mAh g^{-1}, excellent rate-capability, and remarkable long-term cycling stability with a decay rate of only 0.019% per cycle over 1000 cycles at 3 C. This work highlights the importance of precise control in pre-lithiation parameters and the synergistic effects of channel and surface lithium, providing new valuable insights into the design and optimization of SRR electrocatalysts for high-performance LiSBs.

Keywords: Pre-lithiation, Sulfur redox kinetics, Electronic modulation, Drifting effect, Lithium-sulfur battery

1. Introduction

Rechargeable lithium-sulfur batteries are widely recognized as among the promising candidates for next-generation energy storage systems due to their high theoretical energy density of 2600 Wh kg^{-1}, environmentally friendly nature, and low cost. However, despite their potential, the commercialization of LiSBs still faces significant challenges[1–4]. The sluggish kinetics and shuttle behavior originate from the multi-phase and multi-step sulfur redox reaction (SRR), which leads to severe reaction resistance, and ultimately degrades the capacity and rate performances[5,6]. Considerable efforts have been dedicated to developing efficient SRR electrocatalysts with inherent polarity and superior conductivity, aiming to achieve rapid trapping-diffusion-conversion of lithium polysulfides (LiPSs), mitigate the shuttle behavior, and fundamentally address the aforementioned challenges[7–10].

Over the past decades, intense efforts have been made to fundamentally address the shuttle effects and improve the performance of LiSBs[11,12]. Notably, two-dimensional transition metal dichalcogenides (TMDs), such as MoS_2, have attracted considerable attention due to their strong interaction with LiPSs, effectively reducing polarization during the multi-order SRR conversion process[13–15]. As has been reported, the intrinsic conductivity of different MoS_2 phases plays a crucial role in determining electrode electrochemical reactions. It is widely recognized that the trigonal prismatic 2H-MoS_2 exhibits semi-conductive behavior, while the octahedral 1T and 1T' phases are metallic[16,17]. However, unlike the stable 2H phase where two S atoms are aligned, the 1T phase is metastable with two S atoms staggered to form an octahedron configuration and it can be further distorted to form the 1T' phase[18].

The phase transition from 2H to 1T' can be achieved by embedding alkalis into the van der Waals gaps between layers[19,20]. This process not only enhances the electronic structure to mitigate polarization effects but also affects the SRR capability, which is influenced by the concentration of intercalated lithium. However, achieving an optimal level of pre-lithiation is crucial, as insufficient levels prevent the formation of a high ratio of 1T'-MoS_2, while excessive pre-lithiation can result in pulverization,

structural collapse, and degradation of electrochemical performance[21]. Chemical pre-lithiation utilizing organolithium compounds proves to be uncontrollable in practice[22]. Therefore, an elaborate preparation of pre-lithiation catalysts and an in-depth investigation of the molecular-level chemical interactions between pre-lithiation catalysts and sulfur species are required to achieve the desired effects.

In this work, we performed the density functional theory (DFT) calculations[23] to predict that the two pathways in the intercalation of Li^+ ions, namely, along the channels (Li_{ch}) and on the surface (Li_{surf}), play dual roles in SRR. We demonstrated that the synergistic effect of the "electronic modulation effect" by Li_{ch} and the "drifting effect" by Li_{surf} not only modulates the electronic states but also accelerates the multi-step reaction, enabling the high-rate performance and long cycling stability for LiSBs. To precisely regulate the intercalation process, we proposed an electrochemical pre-lithiation approach that achieves the desired amount of lithium intercalation and facilitates the phase transition of MoS_2 from 2H to 1T' phase, in accordance with the intercalation mechanism in lithium batteries. In addition, to further investigate the reaction kinetics of the interfacial reaction, surface charge transfer, and ion diffusion during polysulfide conversions, the distribution of relaxation time (DRT) analysis was employed, which effectively decouples the characteristic processes involved in a typical LiSBs cell[24], providing an in-depth understanding of the catalytic mechanisms of pre-lithiation catalysts in multi-step polarization process. As expected, the as-synthesized 1T'-Li_xMoS_2/CS (pre-lithiated MoS_2 which is heteroepitaxially grown on inner octahedral structure Co_9S_8 core), when utilized in LiSBs, delivers a high initial specific capacity of 1049.8 mAh g^{-1} at 3 C and showcases an impressive rate capability. Furthermore, it demonstrates superb cycling stability with excellent durability, maintaining a minimal decay rate of only 0.019% per cycle over 1000 cycles. These outstanding performance metrics highlight the great potential of the 1T'-Li_xMoS_2/CS electrode as a promising candidate for high-performance LiSBs.

2. Results and discussion

2.1. Density Functional Theory Calculations

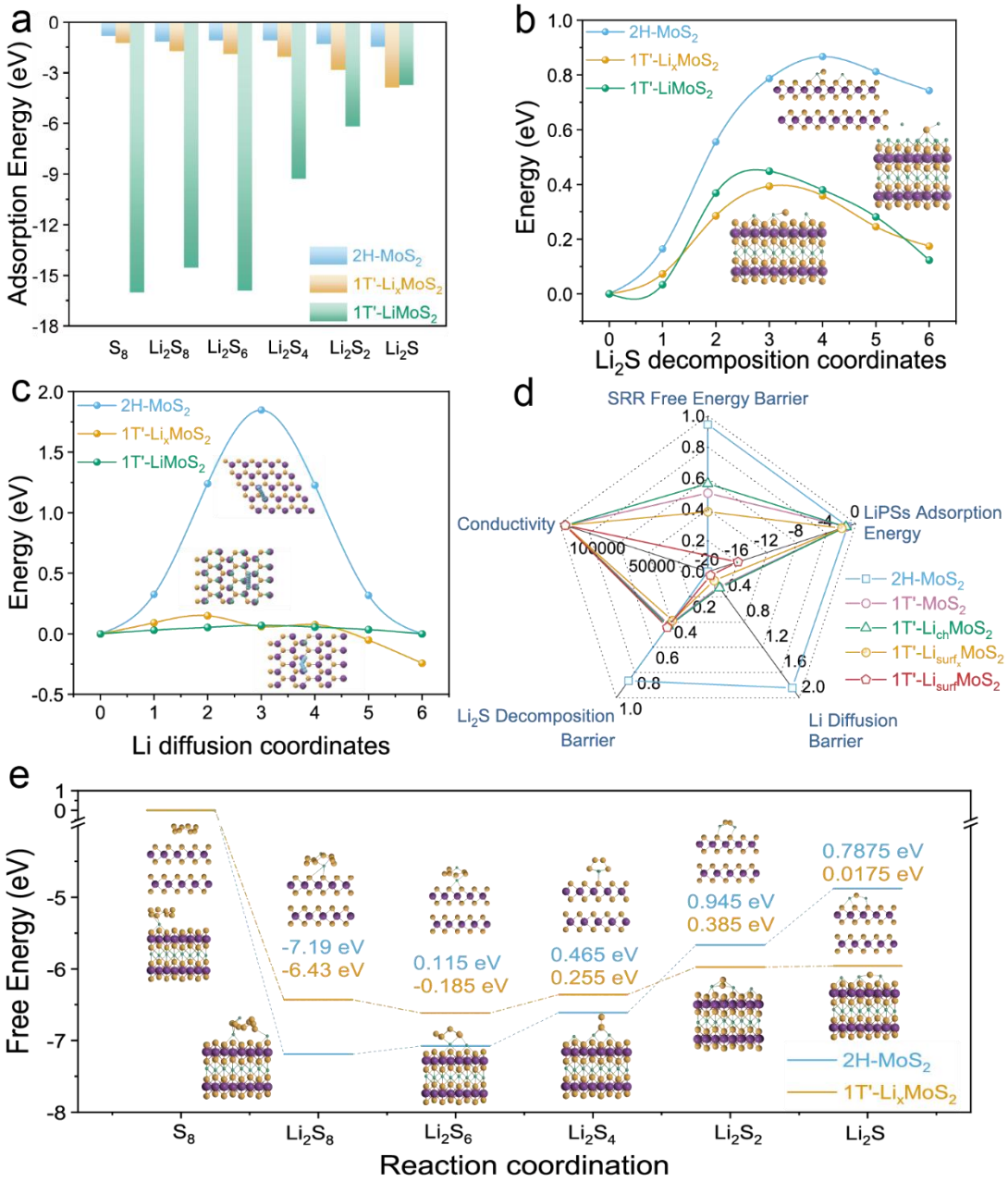

Figure 1. a) Adsorption energy of LiPSs, b) Energy profiles for the Li_2S dissociation (The insets show the configurations at saddle points), c) Energy profiles of lithium-ion diffusion (inset shows the lithium-ion diffusion pathway) and d) Comprehensive parameters related to polysulfide conversion kinetics of original and pre-lithiated MoS_2. e) Free energy diagrams of sulfur reduction reaction on the surface of 2H-MoS_2 and 1T'-Li_xMoS_2 (The insets show the corresponding adsorption configurations). The models in DFT simulations are defined as 2H-MoS_2, 1T'-MoS_2

(1T'-MoS_2 without Li), 1T'-$Li_{ch}MoS_2$ (1T'-MoS_2 with one Li_{ch} layer), 1T'-$Li_{surf}{}_xMoS_2$ (1T'-MoS_2 with one Li_{ch} layer and one isolated Li_{surf} atom on 1T'-MoS_2 (001) surface) and 1T'-$Li_{surf}MoS_2$ (1T'-MoS_2 with one Li_{ch} layer and one Li_{surf} layer on 1T'-MoS_2 (001) surface).

DFT simulations are performed in order to comprehensively understand the kinetics mechanism of SRR and guide the pre-lithiation electrocatalysts design for LiSBs from the point of view of the structure-activity relationship. The models were constructed based on the facts that pre-lithiation induces the phase transition from 2H to 1T' of MoS_2 and that lithium-ions intercalate within the structure. The intercalation pathways of lithium-ions can be divided into two categories: i) on the top surface and ii) along the edge channels, referred to as Li_{surf} and Li_{ch}, respectively (Figure S1)[25]. In particular, the lithium-ions are preferred isolated distribution on the 1T'-MoS_2 surface (Figure S2). The DFT calculations were conducted to investigate five major factors that govern the LiSBs batteries including conductivity, LiPSs adsorption energy, Li_2S decomposition barrier, Li diffusion barrier, and SRR free energy barrier.

The binding energy on different surfaces was calculated to evaluate the surface interactions and immobilization capability of various sulfur species. As shown in Figure 1a, 1T'-Li_xMoS_2 model (1T'-MoS_2 with one Li_{ch} layer and one isolated Li_{surf} atom) exhibits moderate binding strength for various sulfur species, which is stronger than on 2H-MoS_2. The adsorption intensity strength increases with the concentration of Li_{surf} as shown by the green column in Figure 1a, which is attributable to Li_{surf} participating in the immobilization of polysulfides (Figure S1). The excellent adsorption observed cannot be disassociated from the amphipathic sites, including the "sulfiphilicity" sites of Li_{surf} and the "lithiophilicity" sites of surface sulfur atoms of MoS_2. The synergy between these diverse sites contributes to the overall effectiveness of the adsorption process[26,27]. Parallel experiments of Li_2S_6 solutions were carried out to investigate the trapping effect of the Li_{surf} as shown in Figure S4. Significantly, 1T'-$LiMoS_2$ (1T'-MoS_2 with one Li_{ch} layer and one Li_{surf} layer) demonstrates an exceptionally strong binding capacity, especially towards long-chain LiPSs, which prevents their dissolution,

effectively inhibiting the shuttle effect. Besides, the amphipathic sites of 1T'-$LiMoS_2$ are favorable for trapping Li_2S and weaken the strength of the chemical bonds for shearing and dissociation of sulfur species[28,29]. As shown in Figure 1b, due to the electrostatic repulsion of Li_{surf}, Li_2S shows a decomposition barrier of 0.39 eV on 1T'-Li_xMoS_2, which is lower than that on 1T'-$LiMoS_2$ (0.45 eV) and 2H-MoS_2 (0.87 eV), indicating that a fast-charging process takes place on pre-lithiated 1T'-MoS_2.

However, once the polar sites become saturated with sulfur species, subsequent adsorption and conversion reactions are likely to be hindered. The fast Li diffusion and LiPSs transfer rates are essential for achieving rapid charge/discharge kinetics and improving the high-rate capabilities. As shown in Figure 1c, the electrostatic repulsion of Li_{surf} significantly reduces the Li diffusion barrier on 1T'-Li_xMoS_2 (0.15 eV) and on 1T'-$LiMoS_2$ (0.07 eV), both of which are much lower than on 2H-MoS_2 (1.85 eV). Furthermore, the Li diffusion barriers decrease with the increase of Li_{surf} (Figure S3). Hence, Li_{surf} with a high lithium-ion diffusion rate can act as an accelerator through capturing and facilitating the smooth reactions with LiPSs on the catalyst surface, analogous to smoothly drifting along a well-paved road. Here, the rapid refreshing of active sites and the efficient modulation of polysulfide conversion kinetics are collectively termed as "drifting effect".

Importantly, to distinguish roles of surface and channel Li, we compared the performance based on the most important five properties of 2H-MoS_2, 1T'-MoS_2 (1T'-MoS_2 without Li), 1T'-$Li_{ch}MoS_2$ (1T'-MoS_2 with channel Li only), 1T'-Li_{surf_x} MoS_2 (1T'-MoS_2 with one Li_{ch} layer and one isolated Li_{surf} atom) and 1T'-$Li_{surf}MoS_2$ (1T'-MoS_2 with one Li_{ch} layer and one Li_{surf} layer), as illustrated in Figure 1d and Table S1. As can be seen, 2H-MoS_2 (blue dots) has the poorest performance, especially in conductivity, which is five orders of magnitude lower than 1T'-MoS_2 as previously reported[30]. It is predicted that lithium in the channels can transfer freely during the discharge/charge processes, resulting in high ion and intrinsic electron conductivity, a phenomenon defined as the "electronic modulation effect" of Li_{ch}. This effect enables efficient charge storage and transport throughout the cathode. The adsorption energy of

LiPSs is closely related to the concentration of amphipathic sites provided by Li_{surf}. Proper regulation of Li_{surf} is crucial as excessively strong adsorption can hinder catalytic reactions. Moreover, Li_{surf} significantly enhances SRR, Li_2S decomposition, Li diffusion and LiPSs adsorption. The synergistic effect of Li_{surf} and Li_{ch} considerably accelerates both the charging and discharging kinetics and promotes the multi-step sulfur conversion.

Notably, 1T'-Li_xMoS_2 exhibits a significantly lower free energy barrier of 0.39 eV, in a stark contrast to the higher value of 0.95 eV observed for 2H-MoS_2 (Figure 1e), which aligns well with the above discussion. Overall, the DFT calculations highlight the dual roles of pre-lithiation and the distinct contributions of surface and channel Li in enhancing the performance of LiSBs. The insight gained from the DFT study can guide the design and optimization of pre-lithiation electrode materials for high-performance energy storage systems.

2.2. Material Synthesis and Characterization

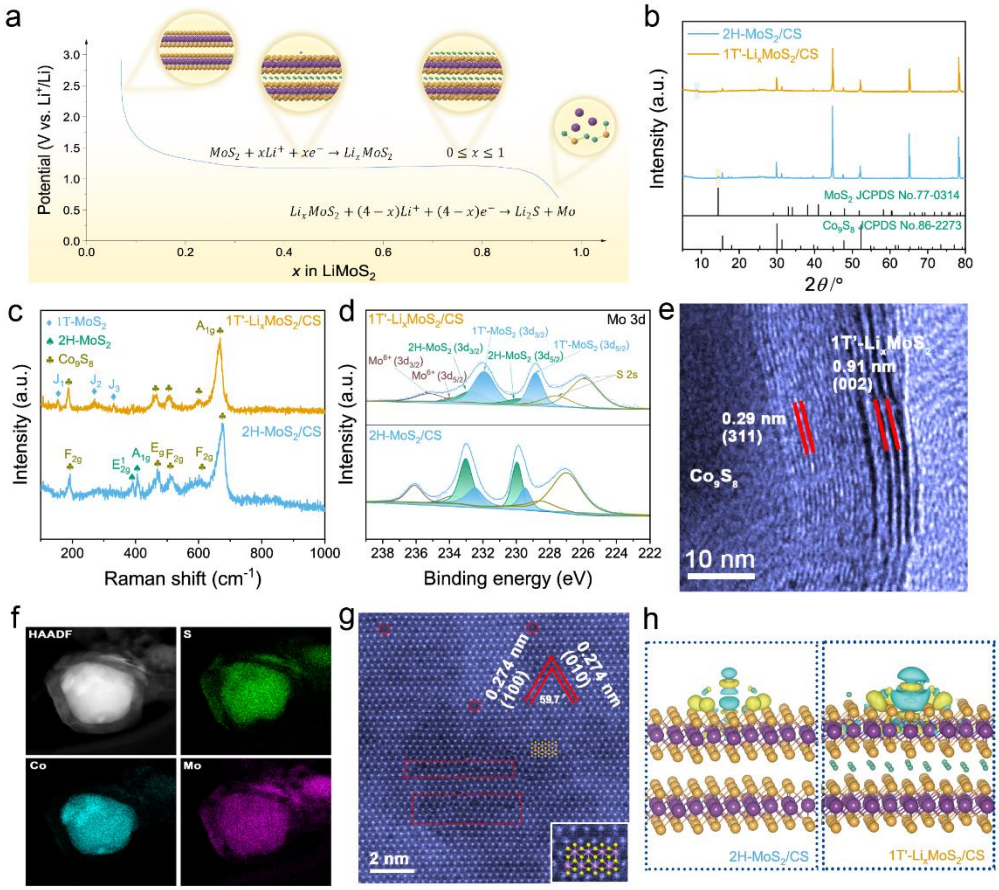

Figure 2. a) Schematic illustration of the electrochemical pre-lithiation process. b) XRD pattern, c) Raman spectra and d) Mo 3d XPS spectra of 2H-MoS_2/CS and 1T'-Li_xMoS_2/CS. e) High-resolution TEM image, f) Mapping images, and g) High-angle annular dark-field transmission electron microscopy (HAADF-STEM) image of 1T'-Li_xMoS_2/CS. h) Charge-density difference plots from the DFT calculations for Li_2S interacting with 2H-MoS_2 (left) and 1T'-Li_xMoS_2 (right), the yellow (blue) distribution corresponds to charge accumulation (depletion).

Building upon the insights gained from the DFT calculations, we developed a precisely controlled pre-lithiation design strategy to validate and further explore the effects of pre-lithiation catalysts in LiSBs. Figure 2a schematically illustrates the dominated pre-lithiation steps of 1T'-Li_xMoS_2/CS. Using 2H-MoS_2/CS as the cathode in the lithium battery, the 1T'-Li_xMoS_2/CS can be facilely obtained through a straightforward in-situ electrochemical method, achieved by accurately adjusting the lithiation depth under an appropriate cutoff voltage. The intercalation of lithium into MoS_2 occurs predominantly during the discharge process within the range of 3–0 V[31].

The distinct plateau observed at 1.2 V corresponds to the intercalation of Li^+ into the van der Waals gaps of 2H-MoS_2 interlayers, resulting in a phase transition from the trigonal prismatic 2H to the octahedral 1T phase, and further to 1T' phase, which is facilitated by electron doping from the intercalated lithium species. Clearly, the 1T phase serves as an intermediate state from 2H to 1T' phase transition[19]. The related electrochemical reaction can be described as following[32]:

$$MoS_2 + xLi^+ + xe^- \rightarrow Li_xMoS_2 \quad (1)$$

where x is in the range of $0 \leq x \leq 1$. The precise control of the cutoff voltage through this electrochemical pre-lithiation strategy enables the regulation of the concentration of intercalated lithium-ions. As depicted in Figure S5, the pre-lithiation process of 2H-MoS_2/CS occurs at nearly 1.2 V, which is much lower than the discharge cut-off voltage of 1.7 V for LiSBs. This observation demonstrates that the 1T' phase can remain stable within the operational voltage range of LiSBs.

In contrast, the excessive lithium intercalation is able to trigger the

disproportionation reaction[21], resulting in severe distortion and subsequent lattice collapse. The related reaction at around 0.5 V can be described as following[33]:

$$Li_xMoS_2 + (4-x)Li^+ + (4-x)e^- \rightarrow Li_2S + Mo \quad (2)$$

According to the above principle, a high cutoff voltage can cause insufficient lithium intercalation and a low ratio of 1T'-MoS_2. Conversely, a low cutoff voltage can lead to structural degradation. Therefore, precise control over the pre-lithiation process is crucial for obtaining the ideal 1T'-Li_xMoS_2 for efficient LiSBs.

To stabilize the phase transition from 2H to 1T' phase process and minimize the curling of the MoS_2 nanosheets, which ensures more active sites to be exposed in the SRR, we synthesized 2H-MoS_2/CS by carefully guiding the heteroepitaxial growth of MoS_2 shells on inner Co_9S_8 cores[34], as shown in Figure S6 and S7. Through a thermodynamic-driven process, the outer MoS_2 shells are able to bond to the inner Co_9S_8 cores via an S atom bridge. This heterointerface not only stabilizes the structure of the pre-lithiated MoS_2 during the charge and discharge process in LiSBs through the Co-S-Mo heterointerface[35] but also facilitates an efficient electron transfer through the built-in electric field. As depicted in Figure S8, CV measurements were conducted in the voltage range of 0.5-2.5 V at a sweeping rate of 0.1 mV s^{-1} to assess the ability of MoS_2/CS and Co_9S_8 to intercalate lithium-ions. Notably, Co_9S_8 demonstrated a more negative intercalation potential compared to MoS_2/CS, suggesting that MoS_2 is more conducive to lithium-ion intercalation than the high crystalline Co_9S_8. The layered structure of MoS_2 gives it a more significant priority in reversible insertion and dissociation of lithium-ions. The crystallographic structure and chemical compositions of pre-lithiation catalysts were analyzed using X-ray diffraction (XRD). As shown in Figure 2b, the distinct peaks at 2 theta angles of 29.7°, 31.2°, and 52.2° match well with the (311), (222) and (440) crystalline planes of cubic-phase Co_9S_8 (JCPDS No. 86-2273)[35]. Three sharp peaks at 2θ of 44.7°, 65.2°, and 78.3° correspond to the aluminum collector (JCPDS No. 85-1327) in the cathode. The diffraction peaks observed at 2θ of ~14° in the 2H-MoS_2/CS can be attributed to the (002) crystalline plane of MoS_2 (JCPDS No. 37-1492). However, upon lithium-ion intercalation, an apparent shift

occurs from 2θ of ~14° to 8.6° in the diffraction pattern of 1T'-Li_xMoS_2/CS, indicating the distortion and expansion of the layer spacing[36]. Undoubtedly, the transformation of the 2H crystal structure to the distorted octahedral 1T' structure and the ultra-thin characteristics of fabricated MoS_2 shell make its XRD intensity much less prominent compared to that of the thicker Co_9S_8 core. In addition, Raman spectra were collected to analyze the chemical constitution and phase structure, as illustrated in Figure 2c. The two typical peaks at 389.7 and 405.5 cm^{-1} were observed, which can be ascribed to the E_{2g}^1 and A_{1g} vibration modes of MoS_2[37], respectively. Besides, the E_g (467.7 cm^{-1}), F_{2g} (193.3, 509.8 and 608.9 cm^{-1}) and A_{1g} (676.2 cm^{-1}) peaks can be attributed to the stretching mode of S-S and the vibrational mode of Co in Co_9S_8[38]. Notably, in comparison to 2H-MoS_2/CS, the Raman spectra of 1T'-Li_xMoS_2/CS show distinct peaks at 153.9, 270.5, and 330.2 cm^{-1}, denoted as J_1, J_2, and J_3, respectively. These representative peaks correspond to the phonon modes of 1T-MoS_2, indicating the phase transition from 2H to 1T'[39]. The chemical states and degree of phase transition after the pre-lithiation process were further investigated by X-ray photoelectron spectroscopy (XPS). The high-resolution Mo3d XPS spectrum of 1T'-Li_xMoS_2/CS (Figure 2d) can be deconvoluted into 1T'-MoS_2 ($3d_{3/2}$ at 231.8 eV and $3d_{5/2}$ at 228.9 eV) and 2H-MoS_2 ($3d_{3/2}$ at 232.7 eV and $3d_{5/2}$ at 229.8 eV). The percentage of the metallic 1T' phase in 1T'-Li_xMoS_2/CS is estimated to be approximately 71.32% based on peak area calculations, confirming the successful attainment of a high ratio of 1T' phase MoS_2 via precise electrochemical control[16,40]. In 1T'-Li_xMoS_2/CS, intercalation of lithium-ions induces significant electronic structure changes, creating a "shielding effect" due to increased electron density around Mo and S atoms, leading to reduced binding energies; meanwhile, binding energy shifts between 2H and 1T' phases are associated with phase transitions, altering the electronic structure and coordination environment.[41–43] Furthermore, the weak peak near 236.0 eV is ascribed to the Mo^{6+} $3d_{3/2}$ as a result of excessive oxidation of Mo, while the peak at 233.3 eV can well be attributed to the reduction of Mo^{6+} to Mo^{5+}[44].

The atomic structure was further investigated by high-resolution transmission

electron microscopy (HRTEM). The inner octahedral structure Co_9S_8 core was hetero-epitaxially bonded with a few layers of MoS_2 shells, forming the MoS_2/Co_9S_8 (MoS_2/CS) core-shell heterostructures (Figure 2e, S7). The inner Co_9S_8 exhibited a distinct lattice fringe with a space of 0.29 nm, corresponding to the (311) plane of the cubic Co_9S_8 phase. Compared to the previously reported well-defined lattice fringe with an interlamellar spacing of 0.65 nm in 2H-MoS_2, the outer MoS_2 shell in 1T'-Li_xMoS_2/CS displayed a degree of distortion and an expanded lattice spacing of 0.91 nm for (002) plane, confirming the pre-lithiation of MoS_2/CS core-shell structures. Next, the corresponding energy dispersive X-ray spectroscope (EDS) provided elemental mappings (Figure 2f), indicating a uniform distribution of MoS_2 shell surrounding the inner polyhedral Co_9S_8 core. The high-angle annular dark-field scanning transmission electron microscopy (HAADF-STEM, Figure 2g) further confirms the existence of the 1T' phase, which matches well with the theoretical atomic structure. The pre-lithiation process created the lattice distortion and abundant defects, which altered the electronic structure and created localized states with unique coordination environments, thus promoting charge transfer and enhancing the activation of adsorbed sulfur species and SRR catalytic activity. To further elucidate the effect of pre-lithiation on the electronic structure of MoS_2, DFT calculation was performed. As shown in Figure 2h, the local charge redistribution induced by pre-lithiation regulates the charge transfer of adsorbed Li_2S, which accelerates the SRR kinetics.

2.3. Electrochemical Performance of Lithium Sulfur Batteries

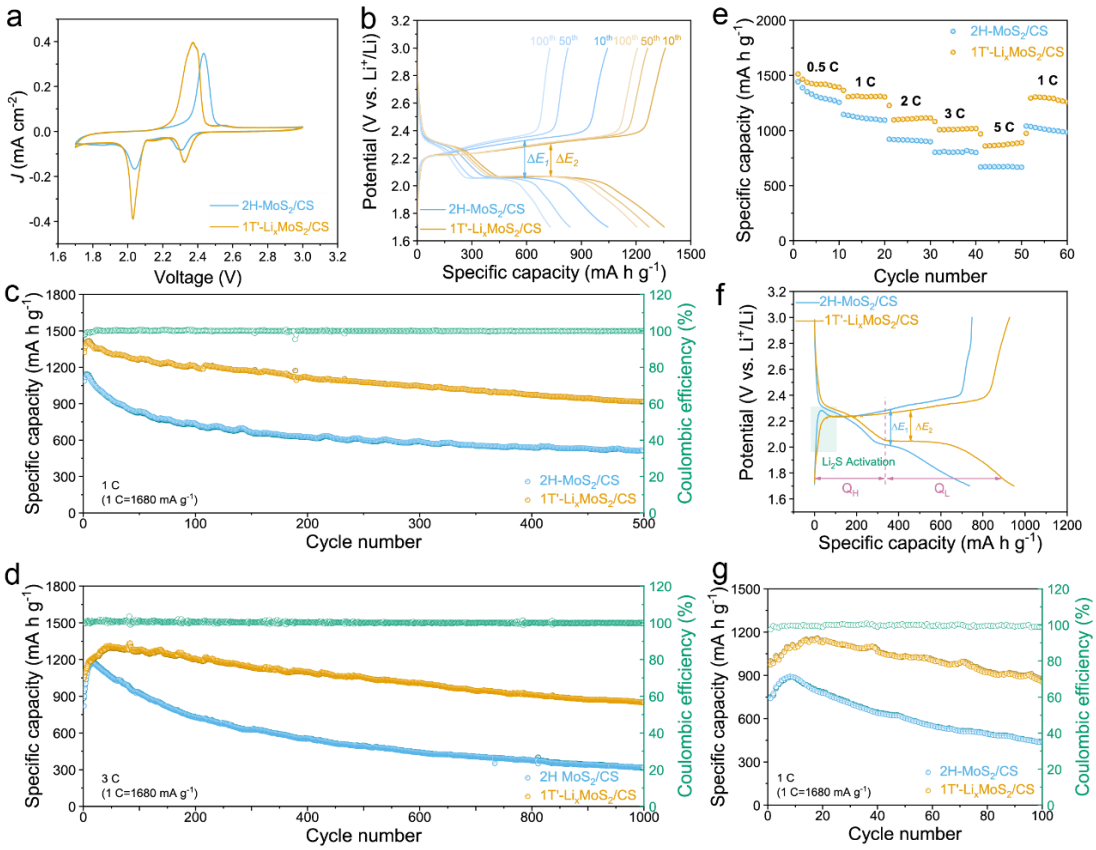

Figure 3. a) Cyclic voltammetry curves of LiSBs. b) GCD profiles after different cycling stages at 1C. c, d) Long-term cycling performance at 1 C and 3 C. e) Rate performance of LiSBs cells. f, g) GCD and cycling performance at 1 C under lean electrolyte conditions.

The theoretical calculations described above indicated that the exceptional ionic conductivity and intricately controlled surface chemistry of 1T'-Li_xMoS_2/CS provide synergistic advantages in regulating sulfur conversion reactions. To verify the effects of pre-lithiation catalysts and assess the optimal regulation design, the electrochemical performance of LiSBs was investigated. As depicted in Figure 3a, cyclic voltammetry (CV) measurements were carried out at a 0.1 mV s^{-1} sweeping rate in the range of 1.7–3.0 V to evaluate the kinetics of sulfur redox reactions under the regulation of 1T'-Li_xMoS_2/CS. The 1T'-Li_xMoS_2/CS-based cell exhibits reduction peaks at 2.32 V and 2.03 V, which are associated with the multi-step reduction of solid S_8 to soluble Li_2S_x ($4 \leq x \leq 8$) and further reduction to solid Li_2S_2/Li_2S, respectively[45]. The considerably higher current density of the reduction peaks indicates the promoted conversion of sulfur species during the solid-liquid-solid process. Meanwhile, the anodic peak

observed at 2.37 V of 1T'-Li_xMoS_2/CS cell is correlated to the oxidation from Li_2S to S_8. A noteworthy observation is that the anodic peak in the 1T'-Li_xMoS_2/CS cell is shifted towards lower potentials in the charge sweep compared to the 2H-MoS_2/CS cell, indicating a reduced overpotential for the solid-solid conversion. Additionally, the CV plot further confirms that there are no new redox peaks observed before and after the pre-lithiation process for the S@2H-MoS_2 and S@1T'-Li_xMoS_2/CS cathode, apart from the typical redox peaks associated with the sulfur redox reaction. All these indicate that there are no marked structural changes and lithium-ions insertion/dissociation for the 1T'-Li_xMoS_2/CS catalysts in LiSBs. As shown in Figure 3b, the voltage plateaus of galvanostatic charge/discharge (GCD) profiles correspond to the peaks in the CV curves. The 1T'-Li_xMoS_2/CS demonstrated the smallest potential interval between the redox peaks and reduced capacity decay, suggesting that the pre-lithiated catalysts facilitate faster SRR kinetics during cycling[46].

To further testify the long-term cycling stability, the cycling performances at 1 C and 3 C were compared, as shown in Figure 3c-d. The 1T'-Li_xMoS_2/CS cell delivers an impressive specific capacity of 1324.76 mAh g^{-1} at 1 C initially, and even after 500 cycles, it maintains a discharge capacity of 916.73 mAh g^{-1}. A slight increase in capacity is observed during the initial cycles, which can be attributed to the sulfur diffusion and electrode activation, resulting in enhanced sulfur involvement in the electrochemical reactions[47,48]. In contrast, the capacity of 2H-MoS_2/CS cathode is much lower and experiences a rapid decay. Besides, the 1T'-Li_xMoS_2/CS can still stably maintain the 1T' phase structure after the long-term cycling (Figure S9). The remarkable cycling performance and stable coulombic efficiency of the 1T'-Li_xMoS_2/CS cell indicate the effective suppression of shuttle effects, which is closely linked to the entrapment of polysulfides and prevention of their dissolution into the electrolyte due to enhanced chemisorption. This is related to the electronic structure modulation by Li_{ch} and charge redistribution induced by the interaction with amphipathic sites (including Li_{surf}) in 1T'-Li_xMoS_2/CS (Figure 2h).

Specifically, even after 1000 cycles, the 1T'-Li_xMoS_2/CS battery maintains a highly reversible capacity of 853.03 mAh g^{-1} with a small capacity degradation of 0.019% per cycle at a high rate of 3 C (Figure 3d). In stark contrast, the 2H-MoS_2/CS battery exhibits a rapid capacity decay, with the capacity continuously dropping to 316.41 mAh g^{-1} with a 0.073% decay rate per cycle over 1000 cycles. The coulombic efficiency of the 1T'-Li_xMoS_2/CS battery remains as high as 99.7% even after 1000 cycles. This corresponds to the high utilization of sulfur. This positions the performance of this battery competitively among the recent publications (Table S3). The excellent reversibility and the long-term cycling performance of 1T'-Li_xMoS_2/CS cathodes along with their high initial capacities at a high current rate can be attributed to the Li_{surf}, which drives the fast redistribution and transfer of active LiPSs species, thus enabling a smooth and rapid conversion of LiPSs through rapid ion transmission.

Notably, the cell with the 1T'-Li_xMoS_2/CS presents a better rate performance than that with a pristine 2H-MoS_2/CS (Figure 3e, S10). The 1T'-Li_xMoS_2/CS cell achieves highly reversible specific capacities of 1480.24, 1310.53, 1104.28, 1011.37, and 864.27 mAh g^{-1} at 0.5C, 1 C, 2C, 3 C, and 5C, respectively, all of which are much higher than those for the 2H-MoS_2/CS. Since 1T'-Li_xMoS_2/CS itself does not directly contribute to the cell capacity, the improved sulfur utilization can be attributed to the kinetic promotion of SRR[47,49]. Upon reverting to a current density of 1 C, the capacity maintains 1295.04 mAh g^{-1} (98.8% of the initial capacity), indicating that the shuttle effect is effectively suppressed, and the sulfur loss is reduced, which results in the reversible and durable capacities of the 1T'-Li_xMoS_2/CS battery at various rates. The impressive capacity retention also underscores the stability and efficiency of the pre-lithiated catalyst in the cell.

To explore the application potential of 1T'-Li_xMoS_2/CS cathodes for practical implementation in LiSBs, the electrochemical performance under the lean electrolyte condition (E/S = 5 μL mg_s^{-1}) with a low lithium conductivity is evaluated (Figure 3f)[50]. The ratio of capacity contribution (denoted as Q_L/Q_H) from the two discharge plateaus is a key kinetic descriptor for the reduction process[51,52]. The higher ratio of Q_L/Q_H

observed for 1T'-Li_xMoS_2/CS indicates an improved efficiency in the conversion of LiPSs-to-Li_2S. Next, the activation energy barrier of Li_2S on as-prepared cathodes was investigated. It was observed that the MoS_2/S cathode exhibited a distinct voltage jump, reaching the highest potential barrier of 2.28 V during the initial charging process[53]. This can be attributed to the semiconducting nature of 2H-MoS_2/CS, which exhibits low electronic conductivity and catalytic activity. Notably, the 1T'-Li_xMoS_2/CS cathode exhibits the lowest potential barrier with the absence of voltage jump peak, indicating an accelerated activation process with a reduced charge transfer resistance[53]. Additionally, 1T'-Li_xMoS_2/CS exhibits the lowest oxidation voltage plateaus and the smallest voltage gap between oxidation and reduction plateaus, indicating highly efficient charge and discharge processes. The smallest polarization can be attributed to the "drifting effect" of Li_{surf}, which accelerates the LiPSs transfer process and enhances the redox kinetics. This further underscores the effectiveness of the pre-lithiated 1T'-Li_xMoS_2/CS electrode in enhancing the performance and stability of lithium-sulfur batteries.

To further evaluate the significance of precise regulation of the pre-lithiation process and gain insights into the correlation between intercalation concentration and SRR kinetics, the discharge depth was controlled with different amounts of lithium-ion intercalation. As shown in Figure S11, the 1T'-$Li_{x2}MoS_2$/CS corresponds to the medium position of the 1.2 V plateau showing the highest specific capacity and the lowest voltage gap of the redox plateau in the GCD profile, indicating the reduced polarization. In addition, the amount of lithium intercalation in the pre-lithiation cell can be determined by calculating and substituting the discharge capacity equivalent to 1 mole of lithium intercalation. Our primary focus is to understand the fundamental mechanisms underlying the dual role of pre-intercalation lithium-ions in LiSBs and gain insights into the relationship between intercalation concentration and SRR kinetics. Rather than aiming for an optimized and precise value for the pre-lithiated ions, our goal is to elucidate the fundamental principles that guide the behavior and performance of these advanced energy storage systems. The moderately pre-lithiated 1T'-

Li_xMoS_2/CS presents superior cycling performance. This result is consistent with the characteristics of 2H phase, which, when there is zero intercalation, displays poor conductivity and thus catalytic activity. The insufficient pre-lithiation induces a lower ratio of phase transition to metallic 1T' phase, which cannot achieve the high-efficient SRR catalysis and suppress the shuttle effect. The over-discharge process leads to the structural collapse of 1T'-Li_xMoS_2/CS, which severely damages the bipolar sites for LiPSs adsorption and the ionic conductivity for LiPSs transfer and conversion, resulting in the lowest coulombic efficiency and significant capacity decay. The above results indicate that the precise regulation of pre-lithiation of 1T'-Li_xMoS_2 results in a remarkable trapping effect and the high SRR catalytic capability toward LiPSs. By reducing the active sulfur loss and accelerating the conversion kinetics of LiPSs, the pre-lithiation process significantly enhances battery performance.

2.4. Sulfur Redox Kinetics Mechanism

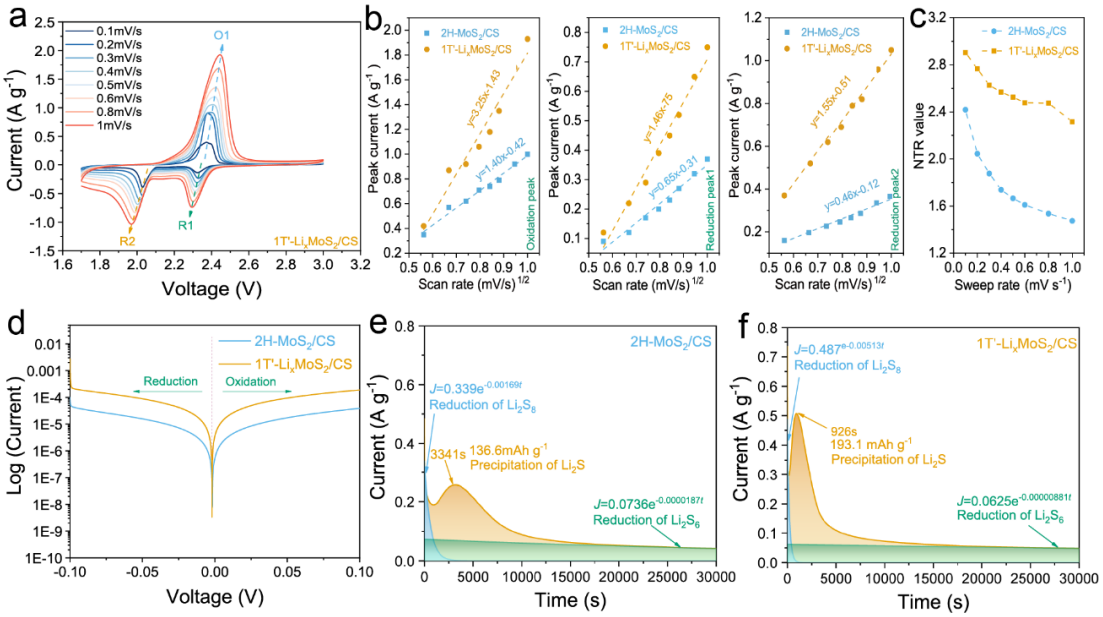

Figure 4. a) CV curves within the voltage range of 1.7–3.0 V at different sweep rates of 1T'-Li_xMoS_2/CS. b) The linear relationship between peak current and square root sweep rate for peak O_1, peak R_1, and peak R_2. c) The NTR values of 2H-MoS_2/CS, and 1T'-Li_xMoS_2/CS at different sweep rates. d) The Tafel plots of the symmetric cells in electrolyte with 0.1 mV s^{-1} from -0.1 to 0.1 V. e, f) Potentiostatic discharge profiles for Li_2S precipitation.

To elucidate the mechanism of the pre-lithiation electrocatalyst boosting the multi-step conversion of polysulfide, the pivotal kinetic parameters were investigated thoroughly. The CV curves of 2H-MoS_2/CS and 1T'-Li_xMoS_2/CS cathodes under different sweep rates (0.1-1 mV s^{-1}) were displayed in Figure 4a and S12. The cathodic peaks observed around 2.3 and 2.0 V correspond to the stepwise reduction from S_8 to Li_2S_6/Li_2S_4 and from Li_2S_4 to Li_2S. The anodic peak around 2.4 V represents the reverse processes. The significantly higher peak current and smaller polarization of 1T'-Li_xMoS_2/CS in CV curves confirm the accelerated redox kinetics, which would be beneficial for the LiPSs transformation. The 1T'-Li_xMoS_2/CS-based cell exhibits steeper slopes at various sweep rates, which are employed to evaluate Li diffusion coefficient (D_{Li^+}) based on Randles-Sevcik equation[17,54]. It can be seen from this equation that I_{peak} varies linearly with the scanning rate v (Figure 4b), so that D_{Li^+} is proportional to the slope of the fitted line and can be calculated according to the slope. The D_{Li^+} values for different electrochemical reaction processes are summarized in Table S2 in the Supporting Information. The 1T'-Li_xMoS_2/CS electrode exhibits an exceptionally high D_{Li^+} value during the electrochemical reactions, facilitating the smooth transportation of LiPSs. This "drifting effect" of Li_{surf} ensures a swift and uninterrupted transfer of LiPSs, preventing their accumulation and thus enabling efficient utilization of active sites, which are favorable for electrochemical conversions of LiPSs.

Since the liquid-solid conversion reaction from Li_2S_4 to Li_2S is recognized as the rate-determining step of SRR process, the nucleation transformation ratio (NTR) is used as an essential indicator. The NTR represents the ratio of the reacted Li_2S_4 in peak R_2 to the produced Li_2S_4 in peak R_1. Thus the ratio provides a measure to evaluate the rate-limiting step of Li_2S_4 reduction[55]. The calculated NTR of the 1T'-Li_xMoS_2/CS cell is closer to 3, which is closer to the ideal conversion conditions from Li_2S_4 to Li_2S (Figure 4c). This is connected to the lower transformation barrier of the short-chain LiPSs and is likely attributed to the fast lithium diffusion, which drives the efficient LiPSs drifting

and conversion on the cathode surface[56]. In contrast, the NTR values of 2H-MoS_2/CS cathodes are less than 2.5 and decrease rapidly with an increase in the scanning rate, indicating that the sluggish kinetics are induced by the accumulation of Li_2S_4, which hinders the conversion to Li_2S.

The Tafel plots derived from linear sweeping voltammetry (LSV) are fitted in the overpotential interval from -0.1 to 0.1 V and are used to evaluate the interfacial reaction kinetics and obtain the exchange-current density (i_0) according to the Butler-Volmer equation[57]. Figure 4d demonstrates that the 1T'-Li_xMoS_2/CS cell exhibits a much higher i_0 compared to 2H-MoS_2/CS, suggesting that the active sites of 1T'-Li_xMoS_2/CS facilitate intrinsic charge transfer kinetics. Considering the superior D_{Li^+} and favorable i_0, the 1T'-Li_xMoS_2/CS is considered highly effective catalytic material for accelerating the reversible electrochemical conversion of LiPSs.

Meanwhile, the liquid-solid conversion process plays a vital role as the capacity-determining step, accounting for approximately 75% of the total theoretical capacity and thereby significantly influencing the overall sulfur utilization in the electrode. Potentiostatic nucleation measurements of Li_2S are explored to deepen the understanding of the enhanced solid-liquid conversion kinetics of LiPSs facilitated by the pre-lithiation electrocatalyst. As depicted in Figure 4e-f, the *I–t* curves are fitted with two exponential functions to create three parts: the reduction of Li_2S_8 and Li_2S_6 (blue and green, respectively), and a peak corresponding to the precipitation of Li_2S (orange)[58]. Specifically, 1T'-Li_xMoS_2/CS-based cell exhibits a more dominant Li_2S nucleation capacity (193.1 mAh g^{-1}) compared to the 2H-MoS_2/CS-based cell (136.6 mAh g^{-1}) (Figure 3e-f). The synergistic effect of Li_{surf} and Li_{ch}, that is, the electronic conductivity and rich refreshing active catalytic sites, is beneficial to enhance the capture ability for LiPSs and efficiently promote the liquid-solid conversion kinetics of Li_2S at the electrode/LiPSs interface, achieving improved discharging capacity.

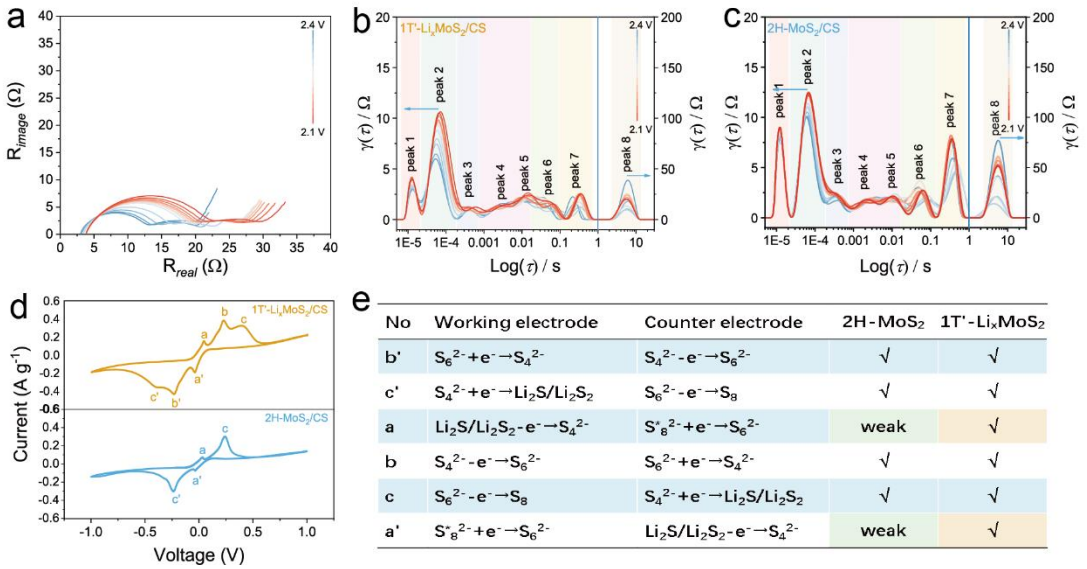

No	Working electrode	Counter electrode	2H-MoS_2	1T'-Li_xMoS_2
b'	$S_6^{2-}+e^-\rightarrow S_4^{2-}$	$S_4^{2-}-e^-\rightarrow S_6^{2-}$	√	√
c'	$S_4^{2-}+e^-\rightarrow Li_2S/Li_2S_2$	$S_6^{2-}-e^-\rightarrow S_8$	√	√
a	$Li_2S/Li_2S_2-e^-\rightarrow S_4^{2-}$	$S^*_8{}^{2-}+e^-\rightarrow S_6^{2-}$	weak	√
b	$S_4^{2-}-e^-\rightarrow S_6^{2-}$	$S_6^{2-}+e^-\rightarrow S_4^{2-}$	√	√
c	$S_6^{2-}-e^-\rightarrow S_8$	$S_4^{2-}+e^-\rightarrow Li_2S/Li_2S_2$	√	√
a'	$S^*_8{}^{2-}+e^-\rightarrow S_6^{2-}$	$Li_2S/Li_2S_2-e^-\rightarrow S_4^{2-}$	weak	√

Figure 5. a) Nyquist plots based on the in-situ EIS under the final charging states from 2.1-2.4 V, b-c) In-situ DRT profiles derived from EIS data under the final charging states from 2.1-2.4 V, and d) CV curves of symmetric cells in 0.25 M Li_2S_8 electrolyte at a sweep rate of 1 mV s^{-1}. e) Schematic of LiPSs catalytic mechanism, where $S^*_8{}^{2-}$ represents the initial polysulfides in the original electrolyte.

The interfacial charge transfer kinetics of the 2H-MoS_2/CS and 1T'-Li_xMoS_2/CS electrodes were further investigated by collecting the in-situ electrochemical impedance spectroscopy (EIS) combined with distribution of relaxation time (DRT) technique analysis. The DRT technique is currently the most widely used method for analyzing impedance information on the time scale[24,59]. The essence of DRT is to transform the EIS Nyquist plots into a distribution on the time scale by convolution. The peak position, height, and area in the DRT plot provide quantitative information about the reaction kinetics and performance-limiting processes.

Figure 5b-c shows the DRT plot derived from the EIS data (Figure 5a, S13), featuring eight local maxima peaks (P1-P8) with distinct time constants, each corresponding to a specific cell process and representing its contribution to the overall polarization resistance. The peak position corresponds to the time constant (τ) of specific polarization processes and regions. The peak area represents the polarization resistance. Therefore, the DRT profile offers more valuable insights into the nature and

magnitude of the electrode reactions. As previously reported[24] , in the high-frequency region, the peaks P1-3 are typically not associated with electrochemical reactions or mass transport. The P1 indicates the ionic resistance and electronic resistance of the electrodes, while P2-3 are attributed to double-layer relaxations and the formation of solid-electrolyte interphase (SEI) at the Li anode. On the other hand, peaks P4-6, identified in the mid-frequency semi-circle, represent the charge transfer behavior of reactions in the cathode region including the formation of the cathode electrolyte interface (CEI) and the multi-electron charge transfer corresponding to the LiPSs conversion[60]. Finally, in the low-frequency region, P7 and P8 can be considered as Warburg impedance arising from the diffusion process. It is worth noting that the presence of two peaks in the diffusion region indicates two distinct ion diffusion regimes. The P7 is predominantly associated with LiPSs diffusion, while P8 is more closely linked to bulk ion diffusion[61].

As shown in Figure 5b-c, the lower intensity of peak P1 in the 1T'-Li_xMoS_2/CS cell is attributed to the semiconductor-to-metallic phase transition and the enhanced ion and intrinsic electronic conductivity facilitated by the Li_{ch}. The peaks P4-6 exhibit a more complex behavior related to the multi-phase and multi-electron conversion of LiPSs. The intensity of P4-6 remains relatively weak in the 1T'-Li_xMoS_2/CS cell during the solid-to-liquid LiPSs conversion process. This observation is consistent with the role of Li_{surf} in mitigating polarization across the entire sulfur redox chemistry, enabling the barrier-free conversion and boosting of the reaction kinetics of LiPSs. Furthermore, the constant smallest intensity of P7 provides further evidence for the crucial role of the Li_{surf}-induced "drifting effect", which contributes to the accelerated LiPSs transfer with negligible resistance. The comprehensive analysis of the DRT plot provides valuable insights into the interfacial charge transfer kinetics and highlights the contribution of different processes to the overall polarization resistance in the 2H-MoS_2/CS and 1T'-Li_xMoS_2/CS cells.

The 1T'-Li_xMoS_2/CS not only demonstrates the ability to capture the LiPSs molecules, but more importantly, exhibits intense electrocatalytic character towards

LiPSs. The accelerated polysulfide redox further affects the series of coupled solid-liquid-solid conversion, as confirmed by the CV profiles of the symmetrical cells. In the symmetrical cells, where 2H-MoS_2 and 1T'-Li_xMoS_2/CS serve as identical electrodes with Li_2S_6-contained electrolytes, the concentrations of Li_2S_x (x = 4, 6, 8) are changed along with the redox reaction during the charge/discharge process (Figure 5d). The CV curve of 1T'-Li_xMoS_2/CS symmetric cell exhibits a high redox reversibility, with three distinct paired redox peaks at -0.04 V/0.37 V (peak a/a'), -0.23 V/0.22 V (peak b/b') and -0.40 V/0.40 V (peak c/c'), respectively. The three reduction peaks in 1T'-Li_xMoS_2/CS cells correspond to the multi-step conversion of soluble Li_2S_6, Li_2S_4, and Li_2S_4 to solid Li_2S_2/Li_2S during the cathodic scan. The paired oxidation peaks indicate the reversible reaction in the counter electrode during the anodic scan[62]. These reaction equations and mechanism derivation are summarized in Figure 5e. The appearance of extra separated paired peaks in the 1T'-Li_xMoS_2/CS cells verifies that the pre-lithiated catalysts significantly enhance the kinetics of long-chain to short-chain liquid LiPSs and the rate-controlled reaction of liquid Li_2S_4 to solid Li_2S_2/Li_2S conversion. This effect is attributed to the "drifting effect" of 1T'-Li_xMoS_2/CS, which accelerates the LiPSs diffusion and catalytic process. In contrast, the lower current value in the 2H-MoS_2 symmetrical cell indicates sluggish kinetics during the multi-step SRR, and the Li_2S decomposition on the surface of 2H-MoS_2 is more challenging. On the other hand, the higher peak current value and the clear peak separation in each redox pair for the 1T'-Li_xMoS_2/CS cell indicate good electrochemical reversibility and facile polysulfide conversion. All of the above observations provide evidence of the significantly enhanced kinetics of polysulfide redox on the 1T'-Li_xMoS_2/CS surface, particularly in the liquid-to-solid phase conversion of Li_2S_4 to Li_2S_2/Li_2S.

3. Conclusion

In summary, this work demonstrates a new conceptual strategy for precisely tuning in pre-lithiated MoS_2/CS to achieve superior LiSBs performance through the "electronic modulation effect" of Li_{ch}, and the "drifting effect" of Li_{surf}. The "electronic

modulation effect" of Li_{ch} enables efficient charge storage and transport throughout the cathode, leading to significantly improved ion and intrinsic electronic conductivity. Simultaneously, Li_{surf} acted as sulfiphilic sites, effectively regulating the surface chemistry and immobilizing LiPSs through amphiphilic polar interactions. Li_{surf} also enables fast ion diffusion and facilitates the rapid and continuous transfer of LiPSs, preventing their accumulation and facilitating the efficient utilization of active sites, thereby reducing the energy barrier for LiPSs conversion and the undesired shuttle process. Consequently, the LiSBs batteries incorporating the 1T'-Li_xMoS_2/CS electrocatalysts exhibit higher specific capacity, improved rate responses, and prolonged cycling lifespan. Furthermore, DFT calculations confirm the low diffusion barrier of lithium-ion, as well as the low SRR free energy barrier and Li_2S decomposition barrier on the surface of 1T'-Li_xMoS_2/CS, aligning with the kinetics analyses. This further confirms the effective catalytic property of 1T'-Li_xMoS_2/CS in LiSBs battery by propelling the kinetic reaction of LiPSs through the "trapping-diffusion-conversion" mechanism. This work not only provides new insights into the precise modulation of pre-lithiated electrocatalysts on the atomic level and systematical investigation of the dual roles of pre-intercalation lithium-ions in SRR, but also highlights a rational design principle for advanced electrocatalysts in the energy-related systems.

4. Experimental section

Preparation of the 2H-MoS_2/CS

In a typical procedure, 0.30 g $Co(NO_3)_2$ and 0.4 g $(NH_4)_2MoS_4$ were dissolved in ethanol and stirred vigorously to obtain a homogeneous solution and dip-coated on a silica substrate. The sulfuration process was carried out by the chemical vapor deposition (CVD) procedure[34]. The as-prepared Mo-Co hybrid precursor was placed in a ceramic boat located at the center of the heating zone of a CVD quartz tube. The sulfur boat was placed at the entrance of the furnace inside the quartz tube as the source. The furnace was heated up to 1000 °C at a rate of 5 °C/min with the Argon flow to

supply the sulfur vapor, and the temperature was held constant for 2 h. After the heat treatment, the heating belt for the sulfur boat was immediately removed, and the furnace was cooled to room temperature.

Preparation of the 1T'-MoS_2/CS

The 2H-MoS_2/CS was fabricated as the cathode material for electrochemical lithium-ion intercalation in the lithium battery. The cathode was prepared by dispersing the 70 wt% of active materials, 20 wt% of super P, and 10 wt% of poly(vinylidene fluoride) (PVDF) in N-methyl pyrrolidinone (NMP) and the mixture was coated on an Al foil. The measured thickness of the electrode is approximately 50 μm (Figure S14). Afterward, the CR2025 coin cell was assembled by using 2H-MoS_2/CS cathode, PP separator (Celgard 2400), Li foil as anode, and 1 M lithium bis(trifluoromethane sulfonyl)imide (LiTFSI) dissolved in DOL/DME (1:1 vol ratio) as the electrolyte in a glove box filled with Ar. The as-prepared coin cell was connected to the Neware battery test system and discharged with a galvanostatic discharge current of 0.05 mA. The cutoff voltage was before the end of the first plateau which was observed around 1.2 V vs. Li/Li^+ in galvanostatic cycling at room temperature. Note that the amount of intercalated lithium-ions was controlled effectively by tuning the cutoff voltage according to the discharge profile. Since the 2H to 1T' phase transition of MoS_2 was associated with the first voltage plateau, we controlled the discharge depth at around 1.2 V plateau to the lithium-ion intercalation of 1T'-MoS_2. The points in the discharge process ending at around the front, middle, and extremity of the first voltage plateau are defined as 1T'-$Li_{x1}MoS_2$, 1T'-$Li_{x2}MoS_2$, 1T'-$Li_{x3}MoS_2$, respectively.

Fabrication of the sulfur cathode.

The S@1T'-$LiMoS_2$ cathode was prepared from the disassembled pre-lithiated battery. The weight of the 1T'-$LiMoS_2$ cathode was recorded. Then a certain amount of 0.5M Li_2S_8 solution in DOL/DME (1:1 vol ratio) was added using a pipette for drop on the as-prepared cathode and further dried at room temperature, corresponding to a sulfur content of 65%. The dropping and drying processes were carried out in an Ar-filled

glovebox. The S@2H-MoS_2/CS cathode was prepared by adding the same amount of 0.5M Li_2S_8 solution in DOL/DME (1:1 vol ratio) on 2H-MoS_2/CS cathode.

Characterization.

The microscopic morphologies were conducted on scanning electron microscopy (SEM, SUPRA 40 Zeiss) and transmission electron microscopy (TEM, JEOL-2100F) at 200 kV. The STEM and EDS mapping experiments were performed on a probe aberration-crorrected transmission electron microscope (Thermofisher Spectra 300) at 200 kV. The convergence angle was set ~ 21 mrad and the range of the detector was set to be ~50 to 200 mrad. The X-ray diffraction (XRD) patterns of the samples were conducted on Bruker D8 Discovery X-ray diffractometer. XPS measurement was performed on Kratos AXIS Supra$^+$ X-ray photoelectron spectrometer (Kratos Analytical Ltd. UK) with a monochromatic Al Kα source, and the C 1s peak (284.8 eV) was used as a reference. The Raman spectra were collected utilizing a Raman microspectrometer (Horiba MicroRaman HR).

Electrochemical Measurements.

The electrochemical performance was evaluated based on standard CR2032 coin-type batteries, which were assembled in an Ar-filled glovebox. The Celgard 2400 membrane, lithium foil and 1 M LiTFSI DOL/DME (1:1 vol ratio) with a 2.0 wt% $LiNO_3$ additive were used as the separator, anode, and electrolyte, respectively. The electrolyte/sulfur (E/S) values were 15 $\mu L_{(electrolyte)}/mg_{(sulfur)}$ for normal conditions, and 5 $\mu L_{(electrolyte)}/mg_{(sulfur)}$ for lean electrolyte conditions. The galvanostatic charge–discharge measurements were performed on a Neware battery test system (NEWARE, CT-4008Tn-5V10mA-HWX) in the voltage range from 1.7 to 3 V versus Li^+/Li. The CV curves and EIS with a signal amplitude of 5 mV ranging from 0.1 MHz to 0.01 Hz frequency were examined on a Solartron 1470E electrochemical workstation (Solartron Analytical, UK)

Li_2S precipitation test.

The coin cells were assembled by adding 20 µL of 0.25 M Li_2S_8 catholyte onto the host materials side and 20 µL of blank electrolyte onto the lithium anode side.

Afterward, the cells were galvanostatically discharged to 2.05 V under a current of 0.112 mA and then maintained at 2.02 V to drive the nucleation of Li_2S until the current was reduced to less than 10^{-5} A.

Symmetric Cell Measurement.

Symmetric cells were assembled with 2H-MoS_2/CS and 1T'-Li_xMoS_2 cathode as electrodes and 0.25 M Li_2S_8 solution in DOL/DME (1:1 vol ratio) containing 1 M LiTFSI as catholyte. The CV curves of symmetric cells were collected from -0.1 V to 0.1 V with a sweep rate of 5 mV s^{-1}.

Supplemented equations.

Lithium-ion diffusion coefficient (D_{Li^+})

D_{Li^+} reflects the LiPSs conversion activity and can be calculated according to the classical Randles–Sevcik equation[54]:

$$I_p = 2.69 \times 10^5 n^{1.5} A D_{Li^+}^{0.5} v^{0.5} C_{Li^+} \quad (3)$$

where I_p represents the peak current, n is the number of electrons transferred during the reaction, A is the geometric area of the cathode electrode, D_{Li^+} is the lithium-ion diffusion coefficient (cm^2 s^{-1}), C_{Li^+} is the concentration of lithium-ion in the electrolyte, and v is the scanning rate (V s^{-1}).

Nucleation Transformation Ratio (NTR)

NTR was defined to comprehensively evaluate the kinetics of polysulfide reduction in LiSBs[55].

The electron transfer numbers C_{ei} (i=1,2) were defined as the following equations:

$$C_{e1} = \frac{A_{t1}}{v} \quad (4)$$

$$C_{e2} = \frac{A_{t2}}{v} \quad (5)$$

where C_{ei} is the amount of electron transfer per gram (A s), A_{ti} is the integral area of peak 1 or peak 2 (A V), and v is the sweep rate (V s^{-1}).

The NTR was evaluated quantitatively for polysulfide conversion capacity by the following equation:

$$NTR = \frac{C_{e2}\ of\ Peak_{R2}}{C_{e1}\ of\ Peak_{R1}} \quad (6)$$

Density functional theory methods

All DFT calculations were performed using Vienna Ab initio Simulation Package (VASP) with the projector-augmented wave (PAW) approach[63–65]. The generalized gradient approximation (GGA) in the form of Perdew-Burke-Ernzerhof (PBE) functional was applied for exchange-correlation interaction and an empirical van der Waals interaction correction using DFT-D3 was employed[66,67]. The convergence tolerances of energy and force were 10^{-5} eV and 0.02 eV/Å, respectively. The transition metal disulfides were simulated with two monolayers. For the channel Li simulation, Li atoms were inserted in between MoS_2 monolayers. For the surface Li simulation, one isolated Li atom and one Li monolayer on the surface were used to represent low-concentration and high-concentration Li insertion, respectively. The climbing image nudged elastic band (CI-NEB) simulations were performed to obtain the barriers of Li diffusion and Li_2S decomposition[68].

The adsorption energies (Eads) are defined as $E_{ads} = E_{total} - E_{sub} - E_{LiPSs}$, where E_{total}, E_{sub} and E_{LiPSs} represent the energies of substrate with LiPSs absorbed, bare substrate and isolated LiPSs, respectively. The SRR process includes 16 lithium ions and electrons transfer from S_8 to Li_2S. The free energy change for each SRR step is evaluated by $\triangle G = \triangle E + \triangle E_{ZPE} - T\triangle S$, where $\triangle E$, $\triangle E_{ZPE}$ and $\triangle S$ represent the difference of electronic energy, zero-point energy and entropy between the higher-order LiPSs and the lower-order LiPSs. The temperature T is set to 300K. The free energy barrier is defined as $\eta = \max\{\triangle G\}$.

Acknowledgments

H. M. Wang, H. Yuan, and W. W. Wang contributed equally to this work. This work is supported by Singapore NRF (NRF-CRP26-2021-0003), research work conducted at the National University of Singapore. Y-WZ and team acknowledge the support from the Italy-Singapore Science and Technology Cooperation (Grant No. R23101R040) and

the Singapore A*STAR SERC CRF Award and the use of computing resources at the A*STAR Computational Resource Centre and National Supercomputer Centre, Singapore.

References

[1] J. W. Choi, D. Aurbach, *Nat. Rev. Mater.* **2016**, *1*, 1.
[2] Y.-X. Yin, S. Xin, Y.-G. Guo, L.-J. Wan, *Angew. Chem. Int. Ed.* **2013**, *52*, 13186.
[3] L. Zhou, D. L. Danilov, F. Qiao, J. Wang, H. Li, R.-A. Eichel, P. H. L. Notten, *Adv. Energy Mater.* **2022**, *12*, 2202094.
[4] J. Sun, T. Wang, Y. Gao, Z. Pan, R. Hu, J. Wang, *InfoMat* **2022**, *4*, e12359.
[5] H.-J. Peng, G. Zhang, X. Chen, Z.-W. Zhang, W.-T. Xu, J.-Q. Huang, Q. Zhang, *Angew. Chem.* **2016**, *128*, 13184.
[6] Q. Pang, X. Liang, C. Y. Kwok, L. F. Nazar, *J. Electrochem. Soc.* **2015**, *162*, A2567.
[7] P. Wang, B. Xi, Z. Zhang, M. Huang, J. Feng, S. Xiong, *Angew. Chem. Int. Ed.* **2021**, *60*, 15563.
[8] X.-Y. Li, S. Feng, M. Zhao, C.-X. Zhao, X. Chen, B.-Q. Li, J.-Q. Huang, Q. Zhang, *Angew. Chem. Int. Ed.* **2022**, *61*, e202114671.
[9] S. Rehman, M. Pope, S. Tao, E. McCalla, *Energy Environ. Sci.* **2022**, *15*, 1423.
[10] J. Sun, H. Yuan, J. Yang, Y.-W. Zhang, J. Wang, *Mater.* **2023**, *1*, 100024.
[11] R. Fang, S. Zhao, Z. Sun, D.-W. Wang, H.-M. Cheng, F. Li, *Adv. Mater.* **2017**, *29*, 1606823.
[12] L. Wang, W. Hua, X. Wan, Z. Feng, Z. Hu, H. Li, J. Niu, L. Wang, A. Wang, J. Liu, X. Lang, G. Wang, W. Li, Q. Yang, W. Wang, *Adv. Mater.* **2022**, *34*, 2110279.
[13] J. Wu, T. Ye, Y. Wang, P. Yang, Q. Wang, W. Kuang, X. Chen, G. Duan, L. Yu, Z. Jin, J. Qin, Y. Lei, *ACS Nano* **2022**, *16*, 15734.
[14] Z. Li, I. Sami, J. Yang, J. Li, R. V. Kumar, M. Chhowalla, *Nat. Energy* **2023**, *8*, 84.
[15] E. Hojaji, E. I. Andritsos, Z. Li, M. Chhowalla, C. Lekakou, Q. Cai, *Int. J. Mol. Sci.* **2022**, *23*, 15608.
[16] Y. Yu, G.-H. Nam, Q. He, X.-J. Wu, K. Zhang, Z. Yang, J. Chen, Q. Ma, M. Zhao, Z. Liu, F.-R. Ran, X. Wang, H. Li, X. Huang, B. Li, Q. Xiong, Q. Zhang, Z. Liu, L. Gu, Y. Du, W. Huang, H. Zhang, *Nat. Chem.* **2018**, *10*, 638.
[17] J. He, G. Hartmann, M. Lee, G. S. Hwang, Y. Chen, A. Manthiram, *Energy Environ. Sci.* **2019**, *12*, 344.
[18] J. Wang, S. Yang, Z. Xu, G. Ai, T. Zhang, W. Mao, *Adv. Mater. Interfaces* **2022**, *9*, 2101699.
[19] S. Yazdani, J. V. Pondick, A. Kumar, M. Yarali, J. M. Woods, D. J. Hynek, D. Y. Qiu, J. J. Cha, *ACS Appl. Mater. Interfaces* **2021**, *13*, 10603.
[20] Y. Zhang, Z. Mu, C. Yang, Z. Xu, S. Zhang, X. Zhang, Y. Li, J. Lai, Z. Sun, Y. Yang, Y. Chao, C. Li, X. Ge, W. Yang, S. Guo, *Adv. Funct. Mater.* **2018**, *28*, 1707578.
[21] R. Yang, L. Mei, Q. Zhang, Y. Fan, H. S. Shin, D. Voiry, Z. Zeng, *Nat. Protoc.*

2022, *17*, 358.
[22] K. C. Knirsch, N. C. Berner, H. C. Nerl, C. S. Cucinotta, Z. Gholamvand, N. McEvoy, Z. Wang, I. Abramovic, P. Vecera, M. Halik, S. Sanvito, G. S. Duesberg, V. Nicolosi, F. Hauke, A. Hirsch, J. N. Coleman, C. Backes, *ACS Nano* **2015**, *9*, 6018.
[23] Q. Liang, S. Wang, Y. Yao, P. Dong, H. Song, *Adv. Funct. Mater.* **2023**, 2300825.
[24] R. Soni, J. B. Robinson, P. R. Shearing, D. J. L. Brett, A. J. E. Rettie, T. S. Miller, *Energy Storage Mater.* **2022**, *51*, 97.
[25] J. Zhang, A. Yang, X. Wu, J. Van De Groep, P. Tang, S. Li, B. Liu, F. Shi, J. Wan, Q. Li, Y. Sun, Z. Lu, X. Zheng, G. Zhou, C.-L. Wu, S.-C. Zhang, M. L. Brongersma, J. Li, Y. Cui, *Nat. Commun.* **2018**, *9*, 5289.
[26] X. Chen, H.-J. Peng, R. Zhang, T.-Z. Hou, J.-Q. Huang, B. Li, Q. Zhang, *ACS Energy Lett.* **2017**, *2*, 795.
[27] W. Yao, W. Zheng, J. Xu, C. Tian, K. Han, W. Sun, S. Xiao, *ACS Nano* **2021**, *15*, 7114.
[28] W. Liu, C. Luo, S. Zhang, B. Zhang, J. Ma, X. Wang, W. Liu, Z. Li, Q.-H. Yang, W. Lv, *ACS Nano* **2021**, *15*, 7491.
[29] J. Sun, Y. Liu, L. Liu, J. Bi, S. Wang, Z. Du, H. Du, K. Wang, W. Ai, W. Huang, *Adv. Mater.* **2023**, *35*, 2211168.
[30] X. Geng, W. Sun, W. Wu, B. Chen, A. Al-Hilo, M. Benamara, H. Zhu, F. Watanabe, J. Cui, T. Chen, *Nat. Commun.* **2016**, *7*, 10672.
[31] T. Stephenson, Z. Li, B. Olsen, D. Mitlin, *Energy Env. Sci* **2014**, *7*, 209.
[32] C. Feng, J. Ma, H. Li, R. Zeng, Z. Guo, H. Liu, *Mater. Res. Bull.* **2009**, *44*, 1811.
[33] X. Fang, C. Hua, X. Guo, Y. Hu, Z. Wang, X. Gao, F. Wu, J. Wang, L. Chen, *Electrochimica Acta* **2012**, *81*, 155.
[34] H. Zhu, G. Gao, M. Du, J. Zhou, K. Wang, W. Wu, X. Chen, Y. Li, P. Ma, W. Dong, F. Duan, M. Chen, G. Wu, J. Wu, H. Yang, S. Guo, *Adv. Mater.* **2018**, *30*, 1707301.
[35] B. Li, Q. Su, L. Yu, J. Zhang, G. Du, D. Wang, D. Han, M. Zhang, S. Ding, B. Xu, *ACS Nano* **2020**, *14*, 17285.
[36] J. Sun, Z. Zhang, G. Lian, Y. Li, L. Jing, M. Zhao, D. Cui, Q. Wang, H. Yu, C.-P. Wong, *ACS Nano* **2022**, *16*, 12425.
[37] X. Fan, P. Xu, D. Zhou, Y. Sun, Y. C. Li, M. A. T. Nguyen, M. Terrones, T. E. Mallouk, *Nano Lett.* **2015**, *15*, 5956.
[38] N. Kornienko, J. Resasco, N. Becknell, C.-M. Jiang, Y.-S. Liu, K. Nie, X. Sun, J. Guo, S. R. Leone, P. Yang, *J. Am. Chem. Soc.* **2015**, *137*, 7448.
[39] Y. Jiao, A. M. Hafez, D. Cao, A. Mukhopadhyay, Y. Ma, H. Zhu, *Small* **2018**, *14*, 1800640.
[40] L. Liu, J. Wu, L. Wu, M. Ye, X. Liu, Q. Wang, S. Hou, P. Lu, L. Sun, J. Zheng, L. Xing, L. Gu, X. Jiang, L. Xie, L. Jiao, *Nat. Mater.* **2018**, *17*, 1108.
[41] Z. Li, X. Mu, Z. Zhao-Karger, T. Diemant, R. J. Behm, C. Kübel, M. Fichtner, *Nat. Commun.* **2018**, *9*, 5115.
[42] P. Zhang, Y. Li, Y. Zhang, R. Hou, X. Zhang, C. Xue, S. Wang, B. Zhu, N. Li, G. Shao, *Small Methods* **2020**, *4*, 2000214.

[43] G. Eda, H. Yamaguchi, D. Voiry, T. Fujita, M. Chen, M. Chhowalla, *Nano Lett.* **2011**, *11*, 5111.
[44] X. Han, X. Tong, X. Liu, A. Chen, X. Wen, N. Yang, X.-Y. Guo, *ACS Catal.* **2018**, *8*, 1828.
[45] W. Yao, C. Tian, C. Yang, J. Xu, Y. Meng, I. Manke, N. Chen, Z. Wu, L. Zhan, Y. Wang, R. Chen, *Adv. Mater.* **2022**, *34*, 2106370.
[46] R. Wang, C. Luo, T. Wang, G. Zhou, Y. Deng, Y. He, Q. Zhang, F. Kang, W. Lv, Q. Yang, *Adv. Mater.* **2020**, *32*, 2000315.
[47] N. Wang, B. Chen, K. Qin, E. Liu, C. Shi, C. He, N. Zhao, *Nano Energy* **2019**, *60*, 332.
[48] R. Fang, S. Zhao, P. Hou, M. Cheng, S. Wang, H.-M. Cheng, C. Liu, F. Li, *Adv. Mater.* **2016**, *28*, 3374.
[49] X. Song, D. Tian, Y. Qiu, X. Sun, B. Jiang, C. Zhao, Y. Zhang, L. Fan, N. Zhang, *Adv. Funct. Mater.* **2022**, *32*, 2109413.
[50] M. Zhao, B. Li, H. Peng, H. Yuan, J. Wei, J. Huang, *Angew. Chem. Int. Ed.* **2020**, *59*, 12636.
[51] C. Zhang, J. J. Biendicho, T. Zhang, R. Du, J. Li, X. Yang, J. Arbiol, Y. Zhou, J. R. Morante, A. Cabot, *Adv. Funct. Mater.* **2019**, *29*, 1903842.
[52] Q. Liu, X. Han, Z. Zheng, P. Xiong, R.-G. Jeong, G. Kim, H. Park, J. Kim, B.-K. Kim, H. S. Park, *Adv. Funct. Mater.* **2022**, *32*, 2207094.
[53] S. Wang, S. Feng, J. Liang, Q. Su, F. Zhao, H. Song, M. Zheng, Q. Sun, Z. Song, X. Jia, J. Yang, Y. Li, J. Liao, R. Li, X. Sun, *Adv. Energy Mater.* **2021**, *11*, 2003314.
[54] G. Zhou, H. Tian, Y. Jin, X. Tao, B. Liu, R. Zhang, Z. W. Seh, D. Zhuo, Y. Liu, J. Sun, J. Zhao, C. Zu, D. S. Wu, Q. Zhang, Y. Cui, *Proc. Natl. Acad. Sci.* **2017**, *114*, 840.
[55] R. Xu, Y. Zhou, F. Wang, H. Tang, Q. Dong, T. Wang, C. Tong, C. Li, Z. Wei, *J. Mater. Chem. A* **2023**, *11*, 657.
[56] R. Xu, H. Tang, Y. Zhou, F. Wang, H. Wang, M. Shao, C. Li, Z. Wei, *Chem. Sci.* **2022**, *13*, 6224.
[57] Q. Pang, C. Y. Kwok, D. Kundu, X. Liang, L. F. Nazar, *Joule* **2019**, *3*, 136.
[58] F. Y. Fan, W. C. Carter, Y.-M. Chiang, *Adv. Mater.* **2015**, *27*, 5203.
[59] Y. Lu, C.-Z. Zhao, J.-Q. Huang, Q. Zhang, *Joule* **2022**, *6*, 1172.
[60] C. Qiu, Y. Hu, K. Cao, X. Wu, B. Huang, J. Liu, Y. Wang, L. Luo, D. Gu, X. Ai, Y. Cao, S. Chen, F. Ke, *Adv. Energy Mater.* **2023**, *13*, 2300229.
[61] E. Barsoukov, J. R. Macdonald, Eds., *Impedance Spectroscopy: Theory, Experiment, and Applications*, Wiley, Hoboken, NJ, **2018**.
[62] H. Lin, S. Zhang, T. Zhang, H. Ye, Q. Yao, G. W. Zheng, J. Y. Lee, *Adv. Energy Mater.* **2018**, *8*, 1801868.
[63] P. E. Blöchl, *Phys. Rev. B* **1994**, *50*, 17953.
[64] G. Kresse, D. Joubert, *Phys. Rev. B* **1999**, *59*, 1758.
[65] G. Kresse, J. Furthmüller, *Phys. Rev. B* **1996**, *54*, 11169.
[66] J. P. Perdew, K. Burke, M. Ernzerhof, *Phys. Rev. Lett.* **1996**, *77*, 3865.
[67] S. Grimme, J. Antony, S. Ehrlich, H. Krieg, *J. Chem. Phys.* **2010**, *132*, 154104.
[68] G. Henkelman, B. P. Uberuaga, H. Jónsson, *J. Chem. Phys.* **2000**, *113*, 9901.